AIP Advances

Numerical analysis of indirect noise generated by compositional inhomogeneities using large eddy simulation

Cite as: AIP Advances **11**, 115103 (2021); https://doi.org/10.1063/5.0065959
Submitted: 06 August 2021 • Accepted: 04 October 2021 • Published Online: 01 November 2021

Y. Gong, W. P. Jones and A. J. Marquis

openaccess

View Online Export Citation CrossMark

ARTICLES YOU MAY BE INTERESTED IN

A combined oscillation cycle involving self-excited thermo-acoustic and hydrodynamic instability mechanisms
Physics of Fluids **33**, 085122 (2021); https://doi.org/10.1063/5.0057521

Multi-frequency sound energy harvesting using Helmholtz resonators with irradiated cross-linked polypropylene ferroelectret films
AIP Advances **11**, 115002 (2021); https://doi.org/10.1063/5.0060305

Transferable room-temperature single-photon emitters in hexagonal boron nitride grown by molecular beam epitaxy
AIP Advances **11**, 115101 (2021); https://doi.org/10.1063/5.0063594



AIP Publishing

© 2021 Author(s).

Numerical analysis of indirect noise generated by compositional inhomogeneities using large eddy simulation

Cite as: AIP Advances 11, 115103 (2021); doi: 10.1063/5.0065959
Submitted: 6 August 2021 • Accepted: 4 October 2021 •
Published Online: 1 November 2021

View Online Export Citation CrossMark

Y. Gong,[a] W. P. Jones, and A. J. Marquis

AFFILIATIONS

Department of Mechanical Engineering, Imperial College London, London, United Kingdom

[a]Author to whom correspondence should be addressed: y.gong@imperial.ac.uk

ABSTRACT

In the present work, indirect noises generated by compositional disturbances in a non-isotropic convergent nozzle are studied using Large Eddy Simulations (LESs). An in-house compressible LES code, Boundary Fitted Flow Integrator-LESc, is utilized to simulate the noise generation in the system. A non-reflective outlet boundary condition is used to eliminate numerical reflections and to ensure the reproduction of the operating conditions in the experiments. The experiments are designed to feature two configurations with different injection positions, which enable the separation of direct and indirect noises. Different operating conditions are investigated, including different injection gases and air mass flow rates. This present paper compares computational results with the experimental measurements. The results revealed that the processes of direct and indirect noise generation are successfully reproduced in the LES, with the noise magnitudes in good agreement with those in the measurements. Injection of gases with smaller (He) and larger (CO_2) molar masses compared to air is found to generate negative and positive indirect noises, respectively, in the LES, which is consistent with the experimental findings. The effect of different air mass flow rates is also investigated and discussed, and the direct noise and indirect noise amplitudes are both found to be closely related to the air mass flow rate.

© 2021 Author(s). All article content, except where otherwise noted, is licensed under a Creative Commons Attribution (CC BY) license (http://creativecommons.org/licenses/by/4.0/). https://doi.org/10.1063/5.0065959

I. INTRODUCTION

Combustion noise is a potential major contributor to aircraft engines and gas turbines, and this has become an increasingly important topic over the last several decades.[1] There are two main categories of combustion noise: direct combustion noise and indirect combustion noise. Direct noise is caused by volumetric expansion and contraction due to unsteady heat released by unsteady combustion. The unsteady heat release rate is also accompanied by temperature and compositional and vortical perturbations, which if accelerated can eventually generate acoustic noise, known as the indirect noise.[2] In real engines, indirect noise is generated at the nozzle or the first stage of the turbine and propagates both downstream and upstream back into the combustor. Those traveling back can contribute to the triggering of thermo-acoustic instability in the combustion chamber[3] and may lead to significant damage to the combustor structure and even engine failure.[4]

Entropy indirect noise caused by temperature perturbations has been a topic for analytical study for over 50 years. Marble and Candel[5] developed one-dimensional transfer functions for the noise generated via an isentropic compact nozzle for different conditions, which laid a foundation for further work on indirect noise generation. The theory was further extended to include a wider range of conditions, and various low-order models have been proposed, e.g., by Goh and Morgans[6] and Christodoulou *et al.*[7] The generation of indirect noise by compositional inhomogeneities was first identified by Ihme[8] and investigated further by Magri *et al.*[9] and Giusti *et al.*,[10] where its importance was quantified in subcritical and supercritical nozzles and the relative contributions were compared with other sources of noise. It has been shown that compositional noise can exceed entropic noise for lean flame conditions and that noise generation in modern low-emission combustors thus requires further study.

Following the above analytical efforts, several model experiments have been devised to investigate the generation of entropic and compositional noises. In the German Aerospace Centre (DLR), an Entropy Wave Generator (EWG) was set up using a heating grid and convergent–divergent nozzle to generate entropic noise

© Author(s) 2021

and the pressure signal was measured downstream for both subsonic and supersonic regimes.[11] Recently, in Cambridge University, an EWG rig has also been set up to investigate indirect noises caused by entropic and compositional inhomogeneities.[12,13] The pressure signal upstream of the nozzle was recorded with various designs, successfully separating and identifying the direct and indirect noises. This work was further extended by De Domenico *et al.*[14] to account for the effect of non-isentropicity on the noise generation by compositional disturbances.

Noise generation has been studied in the DLR EWG of Leyko *et al.*[15] and Duran *et al.*[16] and the Cambridge EWG of De Domenico *et al.*[12–14] using one-dimensional analysis with different models proposed for indirect noise generation. A further step is to take account of the non-uniform distribution of entropic and compositional waves and the dispersion and convection of these waves inside the system: high accuracy simulation, which provides a three-dimensional description of the flow and turbulence, is a natural means whereby this can be achieved. Morgans *et al.*[17] performed incompressible direct numerical simulation (DNS) on a combustor channel flow to investigate the effect of flow advection of entropy waves, where dissipation effects were found to be negligible and that dispersion may not be sufficiently fast. Hence, significant entropy wave strength remained at the combustor exit. Giusti *et al.*[18] applied incompressible Large Eddy Simulations (LES) to study entropy waves and found that the waves decayed as a function of a local Helmholtz number based on the wavelength and axial distance. Moreau *et al.*[19] performed compressible LES of the DLR EWG configuration, successfully reproducing the measured pressure signals and confirmed that the amplitude and shape of the entropy spot (temperature fluctuation caused by the heating device) were distorted, especially when convected over a long distance in the downstream duct, while Rodrigues *et al.*[20] utilized URANS to study the details of entropic and compositional waves generated by thermal and compositional perturbations in an open-end pipe without noise generation. It appears that there have been only a few detailed computational studies of the indirect noise generated by compositional inhomogeneities.

The specific objective of the present work is to investigate the noise generated by compositional perturbations in the Cambridge EWG with a non-isentropic subsonic nozzle. Compressible LES has been performed on the 360° EWG configuration. Different injecting positions, main jet mass flow rates, and injection gases corresponding to the experiments are studied, and the upstream pressure signal is monitored to separate and identify the direct and indirect noises.

This paper is organized in the following manner: The target experiments are described and the basic mechanisms of noise generation and reflection in the EWG configuration are introduced in Sec. II, after which the computational setups together with various computational meshes are outlined in Sec. III. The computed results are presented and compared with experimental measurements with a detailed analysis in Sec. IV. Finally, this paper concludes with the main findings and suggestions for future work.

II. ENTROPY GENERATOR

A. Experimental setup

The target experiments of the present work are a series of test cases conducted with the Cambridge University EWG rig. The experimental configuration is shown schematically in Fig. 1(a) with the key dimensions summarized in Table I. A flow of air with a controlled mass flow rate is fed into the duct through the inlet

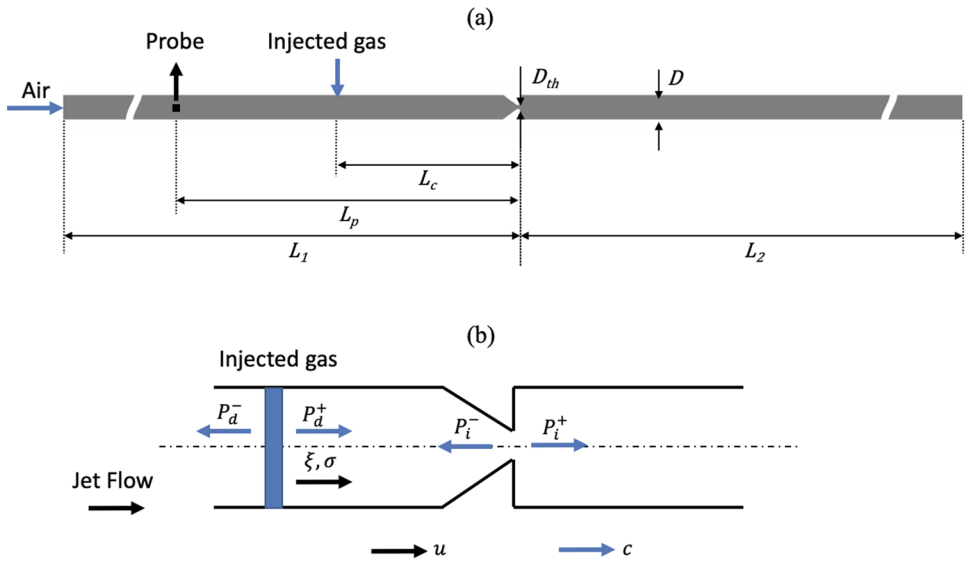


FIG. 1. (a) A simplified layout of the experimental configuration. Specific dimensions are listed in Table I. (b) A schematic diagram of the mechanism of the noise and wave generation and propagation in the system. Acoustic noise, compositional wave, and entropic wave are denoted by P, ξ, and σ, respectively. The subscripts d and i represent direct and indirect noises, and the superscripts + and − represent the propagation directions of the acoustic waves, respectively. The blue arrows represent the acoustic waves propagating at the speed of sound c, and the black arrows denote the jet flow rate at which the compositional and entropic waves travel downstream.

© Author(s) 2021

TABLE I. Dimensions for the experimental configuration.

	L_1	L_2	D	D_{th}	L_p	L_c
Length (m)	1.65	61	0.0426	0.0066	0.75	0.65 or 0.05

on the left of the duct upstream of the nozzle. A pulse of secondary flow is injected perpendicular to the main air flow. The primary air flow is supplied through a long flexible hose, attached via a flat flange to provide a simple acoustic boundary condition. The upstream duct consists of a steel tube with 42.6 mm inner diameter and a length of 1.65 m. A flexible plastic duct is placed downstream of the nozzle, which features the same inner diameter as the upstream tube and a length of 61 m. The reason for such a long duct is to create an anechoic boundary at the outlet. The "round-trip" time for the downstream duct is $2L_2/c = 350$ ms, where c represents the speed of sound. Hence, for $t < 350$ ms, downstream acoustic reflections will not have any effect on the acoustic pressure.[14] In contrast, the inlet boundary has a high reflection coefficient $R_i \approx 0.99$,[13] which is effectively a fully reflective boundary.

In the experiment, two non-isentropic nozzles are employed, namely, convergent and convergent–divergent nozzles, but the present numerical work focuses on the convergent nozzle configuration. The nozzle is 24 mm long featuring a linear geometry profile and a throat diameter of 6.6 mm, followed by the straight downstream pipe. Thus, the flow experiences an abrupt divergence downstream of the converging section, along with flow separations and large losses. Hence, the convergent nozzle terminated with a straight pipe works in a way similar to an orifice plate. A series of measurements were carried out at 11 different air mass flow rates $\dot{m}_a$, and three of these, where the flow in the convergent nozzle is in subsonic conditions, are studied in the present work. The details of test cases considered are presented in Table III. Corresponding to the experiment of De Domenico *et al.*,[14] the injected gas mass flow rates provide a fixed mass fraction of the gas ($Y_{He} = 0.02$ and $Y_{CO_2} = 0.2$) and a similar molar fraction for all cases ($X_{He} \approx X_{CO_2} \approx 0.14$).

B. Pulse injection and noise generation

Pulses of a secondary flow are injected in the cross-stream direction to generate species composition perturbations. Various injected gases are studied, including helium, argon, carbon dioxide, and methane, with each having a different density. Each pulse lasts for $\tau_p = 100$ ms with a 0.25 Hz repetition rate, corresponding to a 4 s period. The mechanism of noise generation in the configuration can be simplified by using a quasi-one-dimensional framework[14] and is depicted in Fig. 1(b). The gas injection has three major effects in terms of the flow fluctuations: first, the injection leads to perturbations in the mass, momentum, energy, and mixture fraction fluxes, generating direct pressure fluctuations that are referred to as direct noise, denoted by P_d (where P represents pressure); these perturbations also cause entropic fluctuations σ, and additionally, compositional fluctuations are caused by the addition of the compositional flux, denoted by ξ. The flow variables can be decomposed into mean and fluctuating values such as $Y_i = \tilde{Y}_i + Y_i'$. In the linear limit when $Y_i' \ll \tilde{Y}_i$, these disturbances do not interact[21] and can be treated as waves with amplitudes related to relative flow variable fluctuations,

$$P^{\pm} = \frac{1}{2}\left(\frac{p'}{\tilde{\gamma}\tilde{p}} \pm \frac{u'}{\tilde{c}}\right), \quad \sigma = \frac{s'}{\tilde{c}_p} = \frac{p'}{\tilde{\gamma}p} - \frac{\rho'}{\tilde{\rho}} - \tilde{\Psi}Z', \quad \xi = Z', \tag{1}$$

where γ, u, c, s, c_p, Z, and Ψ represent the specific heat capacity ratio, velocity, speed of sound, entropy, heat capacity, mixture fraction, and chemical potential function, respectively.[9] Direct noise travels both upstream P_d^+ and downstream P_d^- at the speeds $c - u$ and $c + u$, respectively, approximately equal to the speed of sound c. The entropic and compositional inhomogeneities are convected with the flow downstream toward the nozzle. Once these inhomogeneities are accelerated by the nozzle, indirect noise is generated and propagates both upstream P_i^+ and downstream P_i^- at a speed c. The convective distance L_c represents the distance between the injector and the nozzle and varies with the injection location, with correspondingly different convective time delays $\tau_c = L_c/u$, where u represents the bulk flow speed. Two configurations, based on the injection location, are selected: a long configuration where the injected gas location corresponds to $L_c = 0.65$ m upstream of the nozzle and a short configuration with $L_c = 0.05$ m. In the former case, a separation, τ_c, between the direct and indirect noise arises, whereas in the latter, the direct and indirect noises are almost coincident. By comparing the results of both configurations, the direct and indirect noise contributions can be identified and evaluated, which will be discussed in detail in Sec. IV C.

C. Reverberation

When an acoustic signal is reflected in an acoustic chamber repeatedly over a short period of time, the measured acoustic pressure is effectively an ensemble of the original and all the reflected noise. In the present work, the acoustic "round trip" time in the upstream pipe is $\tau_{round} = 2L_1/\tilde{c} = 2 \times 1.65/340 \approx 0.01$ s. During the injection process, the sound wave in the upstream pipe reflects about $2\tau_p/\tau_{round} \approx 20$ times between the inlet and the nozzle, and this results in reverberation. Hence, the measured upstream pressure signal corresponds to a superposition of the direct noise and its reflections in the upstream pipe between the inlet and the nozzle, which is determined by the direct noise amplitude and the impedance of the boundaries.

III. COMPUTATIONAL METHODOLOGY

A. Compressible BOFFIN-LES

In order to investigate the direct and indirect noise generation, a compressible LES of the Cambridge EWG configuration is performed using the in-house, compressible LES code Boundary Fitted Flow Integrator (BOFFIN-LESc). The pressure-based LES code utilizes the governing equations for compressible flow, including the equation for total enthalpy, and is based on the use of structured multi-block grids. The convection terms in the momentum equations are approximated by a second order central difference scheme, and as such, there is no "numerical" dissipation—at least on a uniform mesh—and it is thus likely negligible. A spatial filtering operation is performed to the governing equations to separate the larger scales from the smaller ones. The unknown sub-grid scale stress arising due to filter operation is approximated via a Smagorinsky sgs viscosity in conjunction with the dynamic procedure of Piomelli and

© Author(s) 2021

Liu.[22] Constant and equal Prandtl and Schmidt numbers with a value of 0.7 are used throughout for both "molecular" and *sgs* fluxes. This is a commonly invoked assumption, and it is not expected to result in significant error. Also at high turbulence Reynolds numbers, the "molecular" transport is overall substantially smaller than the sgs transport. Details of the mathematical formulations can be found in the previous work.[23] BOFFIN-LESc has proven its capability for a variety of turbulent flames,[24,25] including instabilities in complex geometries such as model swirl-stabilized configurations.[26,27]

B. Boundary conditions and grids

The computational domain covers the upstream pipe, nozzle, and part of the downstream pipe. The domain length of the downstream pipe is reduced for cost considerations, with all other dimensions being those listed in Table I. This modification of downstream length is supported by the use of a non-reflective outlet boundary condition,[28,29] with a relaxation coefficient of 0.28,[28] to minimize flow distortion and numerical reflection at the exit. Fully reflective inlet boundary conditions are imposed at the inlet of the pipe to match the experimental impedance discussed in Sec. II A. No-slip adiabatic boundary conditions together with the approximate near-wall, semi-log law based model of Schumann described in Ref. 30 are applied to all solid boundaries. Four meshes are created as listed in Table II. Meshes M1, M2, and M3 cover the same domain with different grid sizes, representing coarse, medium, and fine meshes, respectively. The meshes are smoothly clustered toward the nozzle and throat regions where the minimum mesh spacing exists. For M1, M2, and M3, the minimum mesh sizes are 0.5, 0.25, and 0.15 mm in the axial direction ($\delta^a{}_{\min}$) and 0.5, 0.5, and 0.25 mm for the radial directions ($\delta^r{}_{\min}$), respectively. Mesh M4 is based on M2 but extended to cover a longer domain with a longer downstream pipe with $L_2 = 2.2$ m. This allows the examination of the potential effect of the downstream pipe length on the flow field. Figure 2 shows a sliced view of meshes M1–M4, where different grid sizes and domain lengths can be seen qualitatively. The results of the mesh sensitivity study will be discussed in Sec. IV A.

The present work investigates the effects of different gas injection locations, various air mass flow rates, and injected gases with different molar masses on the noise generations. Helium and carbon dioxide are selected to represent gases lighter and heavier than air, respectively. This leads to eight test cases C1–C8, with details summarized in Table III.

All the simulations are carried out with constant time steps, with the Courant–Friedrichs–Lewy (CFL) number limited below 0.3, and details can be found in the last column of Table III. As shown in Sec. II B, the injection encompasses 100 ms and takes place every 4 s. In the simulations, each case is initialized for one cycle of 4 s after which the data are collected and phase and time averaged. Phase averaging is carried out over two cycles. For each cycle, it was found that after 0.8 s, the pressure level settled to the background level and remains the case until the end of the cycle. Hence, in the simulations, the injection period was reduced to 1 s as a compromise between reliable results and more injection cycles for phase averaging.

TABLE II. Details for computational meshes M1–M4.

Mesh	Cells ($\times 10^6$)	$\delta^a{}_{\min}$ (mm)	$\delta^r{}_{\min}$ (mm)	L_2 (m)
M1	0.08	0.5	0.5	0.35
M2	0.23	0.25	0.5	0.35
M3	0.64	0.15	0.25	0.35
M4	0.42	0.25	0.5	2.2

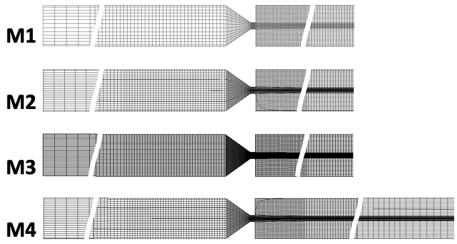


FIG. 2. Slices of numerical grids for M1 coarse mesh, M2 medium mesh, M3 fine mesh, and M4 long mesh.

TABLE III. Numerical conditions for test cases C1–C8: primary mass flow rate $\dot{m}$, injected mass flow rate $\dot{m}_g$, convective distance L_c, and time step Δ_t.

Case	Gas	$\dot{m}$ (gs^{-1})	$\dot{m}_g$ (gs^{-1})	L_c (m)	Δ_t ($\times 10^{-7}$ s)
C1	He	8.0	0.17	0.65	5
C2	He	8.0	0.17	0.05	5
C3	CO_2	8.0	1.62	0.65	5
C4	CO_2	8.0	1.62	0.05	5
C5	He	1.0	0.02	0.65	30
C6	He	1.0	0.02	0.05	30
C7	He	4.0	0.08	0.65	10
C8	He	4.0	0.08	0.05	10

IV. RESULTS AND DISCUSSIONS

A. Reference case

First, a mesh sensitivity study was performed with the mean flow field computed and compared for all four meshes. The flow conditions in C1 are adopted. The flow in each case is initialized for two flow through times after which the time-averaged results are found to be statistically convergent, and then the mean results are collected over another two flow through times. The wall clock time for one flow through time is 24, 50, 96, and 60 h on the Isambard GW4 Tier2 HPC Service (https://gw4.ac.uk/isambard/). Figure 3 shows the mean axial velocity ($\tilde{U}$) profiles along the pipe centerline and diameters at three representative positions, namely, upstream ($x = -200$ mm), throat ($x = 3$ mm), and downstream ($x = 30$ mm). Along the centerline, all simulations exhibit the same low $\tilde{U}$ in the upstream pipe, which increases sharply in the nozzle, reaching a maximum at the throat and then decreasing back to a low downstream bulk velocity. The velocity with M1 reaches a peak $\tilde{U}$ of about 180 m/s, lower compared to the other three simulations, and exhibits a slower decreasing rate downstream of the throat, due to insufficient resolution, while the centerline $\tilde{U}$ on M2, M3, and M4

© Author(s) 2021

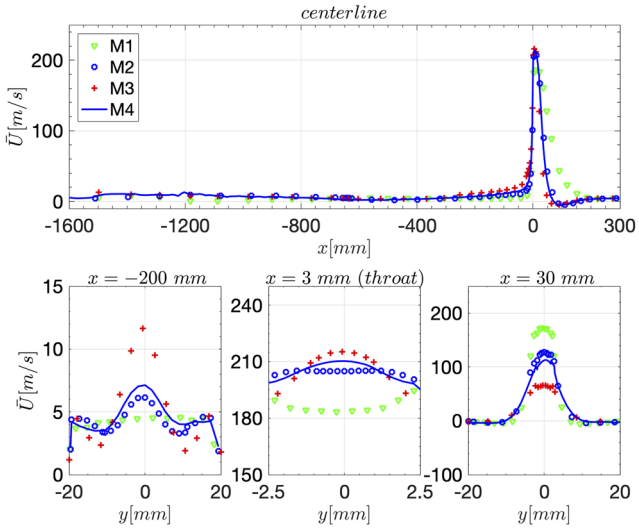


FIG. 3. Mean axial velocities computed from the LES with M1–M4 meshes along the centerline (top) and radial diameters at upstream $x = -200$ mm, nozzle throat $x = 3$ mm, and downstream $x = 30$ mm.

is very similar. In the case of noise generation, the relevant wavelengths lie in the range 1–4 m and the corresponding time scales are 0.003–0.01 s. The maximum mesh size in the axial direction is about 10 mm and around 2 mm in the radial direction. The time step is 2×10^{-7} s, and hence, noise related waves are well resolved by all meshes.

More insights are provided by the radial profiles of $\bar{U}$. First, all radial profiles are closely axisymmetric as is expected. At $x = -200$ mm, the velocity with M3 exhibits a much greater acceleration on the centerline ($y = 0$), which reduces with increasing radius up to half of the pipe radius and increases again from $y = 10$ mm to the solid boundary. The radial profiles with M2 and M4 are very similar but with a much lower peak $\bar{U}$ at the center and a higher "trough" value, while M1 produces generally uniform radial profiles. This difference is almost certainly attributable to the different resolutions of the flow upstream and in the nozzle. In case C1, with the primary mass flow rate $\dot{m} = 8$ gs^{-1}, the Reynolds number is about 6500, which lies within the Reynolds number range where laminar to turbulent transition may occur.[31] The current simulations suggest that the flow is basically in the laminar regime accompanied by some turbulent structures. At the throat, as discussed above, the peak $\bar{U}$ in M1 is much lower compared to the other cases, while M2, M3, and M4 exhibit a similar $\bar{U}$ profile, with a slightly higher peak found in M3, followed by M4 and the lowest is in M2; however, the difference is less than 5% (10 m/s). At the downstream position $x = 30$ mm, which is close to the throat, the lowest $\bar{U}$ is found on M3, followed by M2 and M4, and the highest on M1. This difference is attributed to the more accurate simulation of the losses in the downstream region arising from the finer meshes.

Mean parameters representing the operating conditions are computed and compared with the experimental measurements for the C1 case, including the mean Mach number, M_{th} and M_1, and the mean upstream pressure $\bar{P}_1$, as shown in Table IV. It can be seen that

TABLE IV. Dimensions for the selected cases.

Cases	$\dot{m}$ (gs^{-1})	$\bar{P}_1$ (kPa)	M_{th}	$M_1(\times 10^{-3})$
EXP	8.0	125.4	0.686	11.05
LES_{M1}	8.0	141.8	0.654	12.5
LES_{M2}	8.0	135.4	0.676	12.8
LES_{M3}	8.0	131.2	0.682	12.8
LES_{M4}	8.0	135.6	0.680	12.1

meshes M2, M3, and M4 lead to throat Mach numbers very close to the experimental values, with the best agreement found with M3 and an important indication that the flow field and operating conditions are well captured in the simulations. The mean upstream pressure and Mach number at the upstream probe position are also compared with the measurements. The upstream Mach number of all the cases is very close in every case with less than 15% difference compared to the measurement. At the upstream probe, mesh M1 gives the highest upstream pressure, which indicates the highest loss in the flow,[14] and again, with a finer mesh, better matches between the simulated and measured $\bar{P}_1$ are achieved. M2, M3, and M4 cases show discrepancies of $\bar{P}_1$ below 6%. It can be concluded that the flow properties are, in general, successfully captured in the simulations with meshes M2–M4 to a reasonable accuracy. Given the large axial extend of the EWG configuration and that the focus of the present study is the noise generation and propagation in the region upstream of the nozzle, the medium mesh M2 is selected for the following computational study as a compromise between computing costs and accuracy.

B. Flow field evolution

A flow without radial injection was set up first for each case to initialize the flow field. Figure 4 shows the snapshots of mean axial velocity $\bar{U}$, pressure p, and total pressure p_0 though a slice across the centerline in the nozzle region. The flow is accelerated through the nozzle with the highest velocity $\bar{U}$ occurring at the throat, followed by a "jet" like flow in the downstream pipe. Figure 4(b) shows that the static pressure is almost constant in the upstream pipe and in the nozzle reduces rapidly as the throat approaches its lowest value and then gradually increases to the downstream ambient pressure. Figure 4(c) shows the total pressure that has a constant value in the upstream and with a slight reduction in the nozzle and throat, implying that the flow is almost isentropic in this region. This is not the case when the flow exits the nozzle, where a sudden expansion occurs and the "jet" flow becomes turbulent. Hence, there is a large loss, shown in Fig. 4(c), with a lower total pressure at the nozzle exit, which gradually falls during the mixing with slower moving fluid until no obvious difference can be seen with the surrounding flow.

The injection of the secondary gas in the cross-flow direction is then triggered. Figure 5 shows the evolution of the helium mass fraction snapshots for case C1 from $t = 5$ ms to $t = 300$ ms, where the injection period extends from $t = 0$ ms to $t = 100$ ms. The helium flow enters the pipe at around $t = 5$ ms in the cross-flow direction and then mixes with the main air flow both in the radial and axial directions, after which it is convected downstream toward the nozzle by the main axial flow. At $t = 250$ ms, the helium reaches the nozzle, which gives rise to indirect noise generation as the helium

© Author(s) 2021

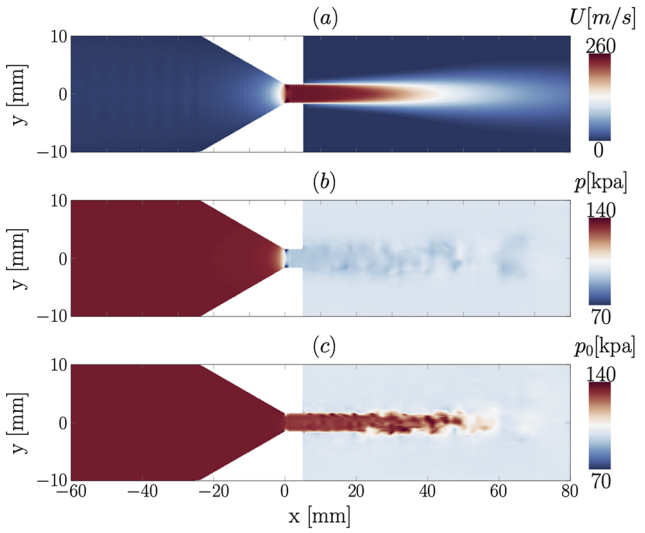


FIG. 4. Sliced color plots of (a) mean axial velocity $\bar{U}$, (b) pressure p, and (c) total pressure p_0 in the region of the nozzle.

wave accelerates in the nozzle. This will be discussed later together with the temporal acoustic noise signal in Sec. IV C.

C. Long pipe configuration

The evolution of non-dimensional pressure fluctuations in the long configuration (L_c = 650 mm) is compared with the experimental measurements, shown in Fig. 6. The pressure fluctuation p' is normalized by the product of the specific capacity ratio $\bar{\gamma}$ and the mean pressure $\bar{p}$. Figures 6(a) and 6(b) show the upstream pressure signals in C1 and C3 with helium and carbon dioxide injected, respectively. The blue lines represent the LES results, while the black solid lines represent the experimental measurements. The red dashed lines are the exponential decay fit of the acoustic energy loss predicted by the reverberation model proposed by Rolland *et al.*[32]

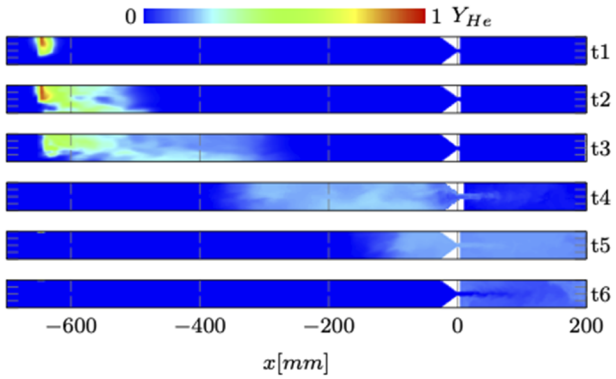


FIG. 5. Temporal evolution of the helium mass fraction in C1 on slice across the pipe centerline at $t1$ = 5 ms, $t2$ = 50 ms, $t3$ = 105 ms, $t4$ = 165 ms, $t5$ = 250 ms, and $t6$ = 300 ms.

The injection lasts for 100 ms and ends at $t = \tau_p$, during which time the acoustic p' rises rapidly and reaches a maximum at $t = \tau_p$. This corresponds to the acoustic waves generated as a direct result of the gas injection and reverberation effects. After reaching the maximum value, the pressure signal begins to fall due to the loss of acoustic energy. Both the measured and simulated p' decay exponentially and follow the decay fit line up to $t = \tau_c \approx 163$ ms when the injected gas reaches the nozzle, as shown in Fig. 5 at t = 165 ms. At $t = \tau_c$, the injected gas reaches the nozzle where it is accelerated, generating indirect noise that propagates upstream toward the probe (P_i^-, Fig. 2). Hence, p' begins to deviate from the decay fit curve in both the measurements and LES. In case C1, the indirect noise is negative, while in C3 it is positive, which is due to the relative molar masses of He and CO_2 compared to air. The indirect noise reaches a maximum at around t = 0.26 s, which is close to the time where the compositional wave is fully convected through the nozzle. This is supported by the fact that t = 0.27 s is very close to the summation of pulse injection time and convective delay $\tau_c + \tau_p \approx 0.263$ s. On comparison of the measurements and LES p' profiles up to t = 0.16 s, it can be observed that the peak amplitudes, arrival times, and the shapes of the p' signal are well reproduced by the LES, suggesting strongly that the time histories of the compositional disturbance source are well defined and the acoustic boundary conditions are determined appropriately.

In the case of the indirect noise, both the measurements and LES p' begin to deviate from the theoretical decay model at around t = 165 ms with the time of the indirect noise generation being well reproduced by the LES, implying that the bulk convective velocities are accurately computed. However, the indirect noise is slightly under-predicted in C3 with CO_2 injection. This is largely due to the over-prediction of the loss in the flow suggested by a higher upstream pressure and therefore the mismatch of the throat Mach number and upstream pressure as discussed in Sec. IV A. More discussions are provided in Sec. IV E. This will affect the computed indirect acoustic source strength and the reflections at the nozzle and is found to be related to the molar mass of the injected gas. In addition, the acoustic signature has been found to be related to the convection process and dispersion effect in the upstream pipe,[20] although this effect should be small in the present case with a very small Helmholtz number, which reflects the nozzle compactness. To further investigate this, a finer mesh is required to simulate the compositional and entropy wave propagation and dispersion and the flow across the nozzle.

D. Short pipe configuration

In the short pipe configuration, the cross-stream gas is injected very close, 50 mm, to the nozzle corresponding to a convective time delay of the compositional and entropic wave of $t = \tau_c \approx 0.001$–0.01 s, which is very short compared with the pulse duration $t = \tau_p$ = 0.1 s, as indicated in Fig. 7. This suggests that the direct noise and indirect noise are generated almost simultaneously. In contrast to the long configuration cases discussed above, where the direct noise and indirect noise are separated, the two sources of noise largely overlap in the short configuration. Figures 7(a) and 7(b) show the upstream pressure signals for cases C2 and C4. From t = 0 to $t = \tau_c$, there is only direct noise present and p' increases as a consequence. Between $t = \tau_c$ and $t = \tau_p$, indirect noise is also generated,

© Author(s) 2021

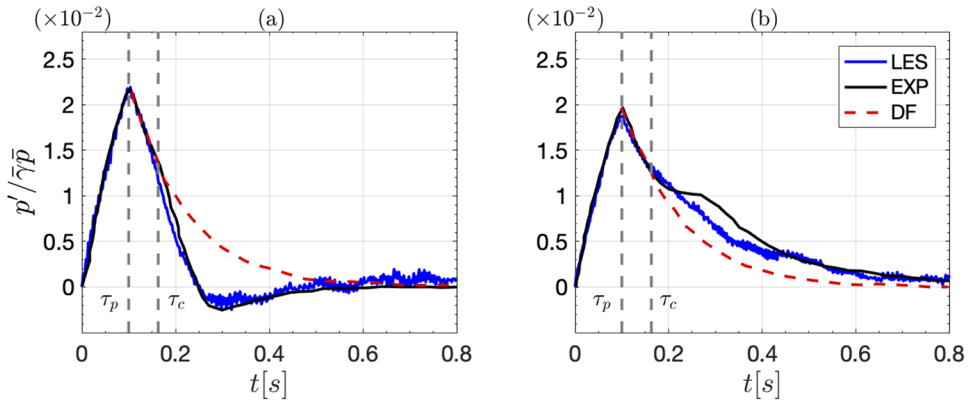


FIG. 6. Phase averaged, normalized acoustic pressure fluctuations in the long pipe configuration at the upstream probe: (a) C1 with He injection and (b) C3 with CO_2 injection. The blue line represents the LES results, while the black solid line represents the experimental measurements. The red dashed line denotes the exponential decay fit of the acoustic energy loss in theory.[14] Two vertical dashed lines mark the end of the injection duration τ_p and convective time of the compositional waves $\tau_c \approx 163$ ms.

and p' represents the acoustic perturbation as a combined effect of the direct and indirect noise. Beyond τ_p, there is only indirect noise present in the pipe, while after $t = \tau_p + \tau_c$, no noise is generated and the acoustic pressures decay until all the acoustic energy is dissipated.

On observing Figs. 6 and 7 together and comparing the maximum p' at τ_p for C1 in Fig. 6(a) and C2 in Fig. 7(a), it can be found that the peak p' is much smaller by about 50% in the short configuration, caused by the negative indirect noise. In contrast for the CO_2 cases, with positive indirect noise, the maximum p' is higher in case C4 shown in Fig. 7(b) compared to that for C3 in Fig. 6(b), consistent with the positive indirect noise found in the long configuration. Since p' maxima represent the direct noise amplitudes in the long configuration and the superposition of direct noise and indirect noise amplitudes in the short configuration, the results can be used to estimate the ratio, k, of the indirect to direct noise. The simulated ratio is $k = 0.46$ for He and $k = 0.19$ for CO_2 compared with the values obtained from the measurements of about 0.42 for He and 0.27 for CO_2. Thus, the simulated indirect noise is lower by about 9% for He and 26% for CO_2 than the values obtained from the measurements.

E. Influence of mass flow rate

Pressure signals with different air mass flow rates are studied with LES for both the long and short pipe configurations. As discussed in Sec. IV B, an air flow is set up in each case. The upstream pressure in cases with different mass flow rates can be used to investigate the isentropicity of the nozzles using the total pressure loss coefficient, which can be expressed as follows:

$$C_{p0} = \frac{p_{0,j} - p_{0,2}}{1/2\rho_j u_j^2} = \frac{p_{0,1} - p_{0,2}}{1/2\rho_j u_j^2}, \tag{2}$$

where C_{p0} is a normalized pressure loss coefficient and p_0 is the total pressure and where the subscripts 1, 2, j represent the upstream, downstream, and position where the flow just begins to become non-isentropic. A non-isentropicity parameter β is introduced to indicate

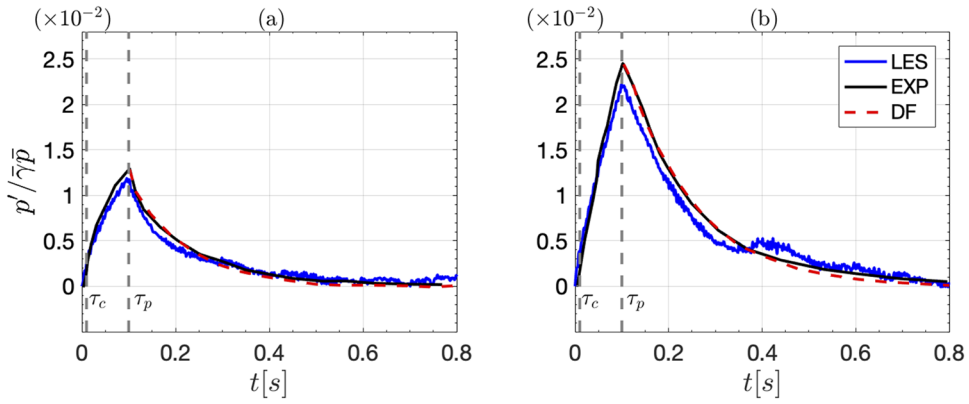


FIG. 7. Normalized acoustic pressure fluctuations in the short pipe configuration at the upstream probe: (a) C2 with He injection and (b) C4 with CO_2 injection.

© Author(s) 2021

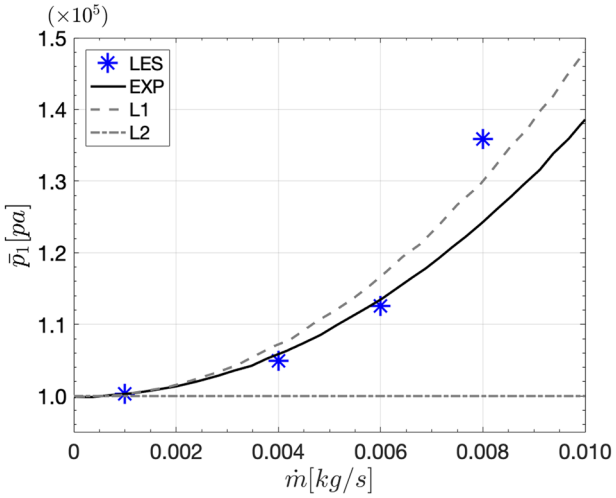


FIG. 8. LES predicted upstream pressure $\bar{p}_1$ vs mass flow rate compared with experimental measurements. Two analytical limits are presented with L1 for the orifice plate limit and L2 for a fully isentropic nozzle.

the level of total pressure losses occurring in the system, which is defined as $\beta = A_j/A_2$, where A represents the cross-sectional area.[33] Hence, according to the definition of β, two limits can be given: when the flow is fully isentropic, $C_{p0} = 0$ and $\beta = 1$; when A_j equals the throat area A_t, the highest loss occurs in the nozzle, and hence, $\beta = A_t/A_2$. The latter case corresponds to the configuration of an orifice plate with the same throat area A_t. As discussed in the work of De Domenico *et al.*,[33] for a given geometry and mass flow rate, each value of β corresponds to a specific upstream pressure $\bar{p}_1$ and to a specific mean pressure loss. The pressure $\bar{p}_1$ as a function of air mass flow rate $\dot{m}$ obtained by LES and the experiments is shown in Fig. 8. The two limits of isentropic flow (L2) and orifice plate (L1) predicted by the analytical model[14] are also depicted. As shown in Fig. 8, the basic trend of $\bar{p}_1$ rising with $\dot{m}$ is captured well by the LES. The value of $\bar{p}_1$ is well predicted in C1, C4, and C6 but is over-estimated in C8, slightly higher than the $\bar{p}_1$ given by the theory for an orifice plate with the same mass flow rate. This indicates larger losses in the simulation when the flow rate is high and the Mach number in the nozzle is close and above unity. The larger discrepancy in $\bar{p}_1$ may be associated with the occurrence of shocks in the vicinity of the sudden expansion downstream of the nozzle, and in these circumstances, the accuracy of Boffin-LESc is uncertain.

Figure 9(a) presents the upstream non-dimensional pressure fluctuations for C1 ($\dot{m}$ = 8 gs^{-1}), C5 ($\dot{m}$ = 4 gs^{-1}), and C7 ($\dot{m}$ = 1 gs^{-1}) based on the long pipe configuration, while Fig. 9(b) shows the results in C2, C6, and C8 where the jet mass flow rates are the same as in C1, C5, and C7, respectively, but the short pipe configuration is adopted. In Fig. 9(a), the direct noise amplitude (represented by the normalized peak p') reduces from C1 to C7. This can be explained using the one-dimensional simplified theory.[14] As discussed in Sec. II B, the secondary gas injection causes perturbations in mass, momentum, energy, and mixture fraction fluxes. Given the fact that the perturbations have a low frequency ($f_p < 1$ Hz), the entropy generator is assumed to be compact compared to the wavelengths of interest ($\lambda \approx 1$–4 m). Hence, a jump condition holds whereby mass, momentum, energy, and mixture fraction fluxes are added to the flow at a discontinuity, and the mean flow properties are assumed to be conserved across the discontinuity. The normalized changes in mass, momentum, energy, and mixture fraction are denoted by $\phi'_m, \phi'_M, \phi'_e$, and ϕ'_Z, respectively, and are defined as

$$\phi'_m = \frac{\Phi'_m}{\bar{\rho}\bar{u}}, \quad \phi'_M = \frac{\Phi'_M}{\bar{\rho}\bar{u}^2}, \quad \phi'_e = \frac{\Phi'_e}{\bar{\rho}\bar{u}\bar{c}_p}\tilde{T}_T, \quad \phi'_Z = \Phi'_Z. \tag{3}$$

In cases C1, C5, and C7, ϕ'_m and ϕ'_Z have the same values since Y_{He} is held constant; therefore, a higher injection mass flow rate causes a higher level of momentum (ϕ'_M) and energy (Φ'_e) perturbations, which leads to a higher peak amplitude of the direct noise shown in Fig. 9(a). An estimation of the ratio of indirect noise to direct noise k can be obtained using the method outlined in Sec. IV C and are listed in Table V: $k \approx 0.11$ for $\dot{m}$ = 1 gs^{-1} for cases C7 and C8, $k \approx 0.37$ for $\dot{m}$ = 4 gs^{-1} for cases C5 and C6, and $k \approx 0.46$ for $\dot{m}$ = 8 gs^{-1} for cases C1 and C2. Since the normalized compositional perturbations are the same in all the cases, the changes in the indirect noise amplitude are mainly due to the increased entropic noise

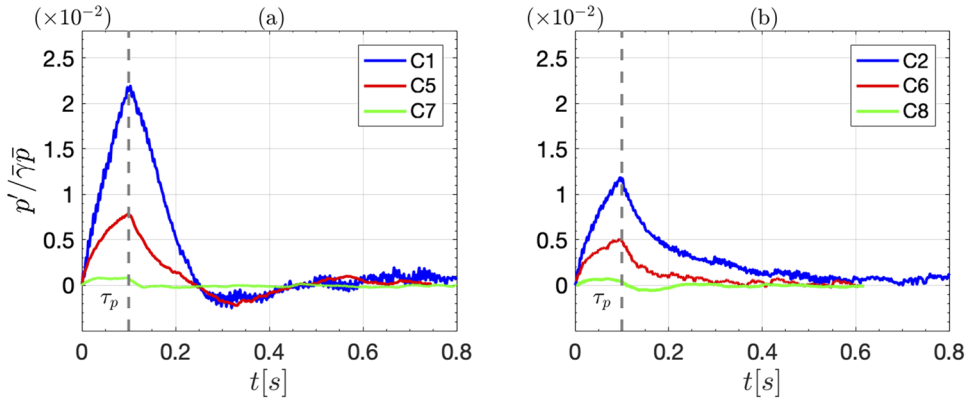


FIG. 9. Normalized acoustic pressure fluctuations in the (a) long configuration and (b) short configuration caused by injections of three different He mass flow rates. The legends show the test cases in each plot, and detailed conditions of each case are shown in Table III.

© Author(s) 2021

TABLE V. An estimation of the ratio of indirect noise to direct noise k.

$\dot{m}$ (gs^{-1})	Cases	k
1	C7, C8	0.11
4	C5, C6	0.37
8	C1, C2	0.46

caused by a higher level of momentum and energy perturbations arising from higher injection mass flow rates.

V. CONCLUSIONS

The present paper describes the results of a numerical study of the noise generation by compositional perturbations in a non-isentropic nozzle. A fully compressible LES is performed for the full 360° EWG configuration, with an appropriate choice of boundary conditions and computational domain. The compositional inhomogeneities are generated by a cross-flow pulse injection. The pressure signal extracted from the LES reproduced the direct and indirect noise generating process and matched the measurements to a good level of accuracy for different injection gases. Cases with different air mass flow rates were also investigated, and these show that the simulation captures the isentropicity of the nozzle flow with an over-prediction for the case with the highest mass flow rate. The effect of increasing main flow mass flow rate on noise generation is also studied and discussed in relation to an analytical method. The indirect noise amplitude and upstream pressure are found to be closely related to the losses in the system, which are higher in the simulation when the Mach number in the nozzle approaches unity and shocks may exist. Under these circumstances, the accuracy of the numerical method is uncertain and requires further investigations.

ACKNOWLEDGMENTS

This research was funded by Imperial College London and the China Scholarship Council (CSC) (Grant No. 201708060199). This work was supported by the Engineering and Physical Sciences Research Council (EPSRC) (Grant Nos. EP/K026801/1 and EP/R029369/1) through the UK Consortium on Turbulent Reacting Flow (UKCTRF). The simulations have been performed using the ARCHER2 UK National Supercomputing Service (http://www.archer2.ac.uk) and the Isambard GW4 Tier2 HPC Service (https://gw4.ac.uk/isambard/).

AUTHOR DECLARATIONS

Conflict of Interest

The authors have no conflicts to disclose.

DATA AVAILABILITY

The data that support the findings of this study are available from the corresponding author upon reasonable request.

REFERENCES

[1] A. P. Dowling and Y. Mahmoudi, "Combustion noise," Proc. Combust. Inst. **35**, 65–100 (2015).
[2] M. S. Howe, "Indirect combustion noise," J. Fluid Mech. **659**, 267–288 (2010).
[3] A. S. Morgans and I. Duran, "Entropy noise: A review of theory, progress and challenges," Int. J. Spray Combust. Dyn. **8**, 285–298 (2016).
[4] T. Poinsot, "Prediction and control of combustion instabilities in real engines," Proc. Combust. Inst. **36**, 1–28 (2017).
[5] F. E. Marble and S. M. Candel, "Acoustic disturbance from gas non-uniformities convected through a nozzle," J. Sound Vib. **55**, 225–243 (1977).
[6] C. S. Goh and A. S. Morgans, "Phase prediction of the response of choked nozzles to entropy and acoustic disturbances," J. Sound Vib. **330**, 5184–5198 (2011).
[7] L. Christodoulou, N. Karimi, A. Cammarano, M. Paul, and S. Navarro-Martinez, "State prediction of an entropy wave advecting through a turbulent channel flow," J. Fluid Mech. **882**, A8 (2020).
[8] M. Ihme, "Combustion and engine-core noise," Annu. Rev. Fluid Mech. **49**, 277–310 (2017).
[9] L. Magri, J. O'Brien, and M. Ihme, "Compositional inhomogeneities as a source of indirect combustion noise," J. Fluid Mech. **799**, R4 (2016).
[10] A. Giusti, L. Magri, and M. Zedda, "Flow inhomogeneities in a realistic aeronautical gas-turbine combustor: Formation, evolution, and indirect noise," J. Eng. Gas Turbines Power **141**, 011502 (2018).
[11] F. Bake, C. Richter, B. Mühlbauer, N. Kings, I. Röhle, F. Thiele, and B. Noll, "The entropy wave generator (EWG): A reference case on entropy noise," J. Sound Vib. **326**, 574–598 (2009).
[12] F. De Domenico, E. O. Rolland, and S. Hochgreb, "Detection of direct and indirect noise generated by synthetic hot spots in a duct," J. Sound Vib. **394**, 220–236 (2017).
[13] E. O. Rolland, F. De Domenico, and S. Hochgreb, "Direct and indirect noise generated by entropic and compositional inhomogeneities," J. Eng. Gas Turbines Power **140**, 082604 (2018).
[14] F. De Domenico, E. O. Rolland, J. Rodrigues, L. Magri, and S. Hochgreb, "Compositional and entropy indirect noise generated in subsonic non-isentropic nozzles," J. Fluid Mech. **910**, A5 (2021).
[15] M. Leyko, S. Moreau, F. Nicoud, and T. Poinsot, "Numerical and analytical modelling of entropy noise in a supersonic nozzle with a shock," J. Sound Vib. **330**, 3944–3958 (2011).
[16] I. Durán, S. Moreau, and T. Poinsot, "Analytical and numerical study of combustion noise through a subsonic nozzle," AIAA J. **51**, 42–52 (2013).
[17] A. S. Morgans, C. S. Goh, and J. A. Dahan, "The dissipation and shear dispersion of entropy waves in combustor thermoacoustics," J. Fluid Mech. **733**, R2 (2013).
[18] A. Giusti, N. A. Worth, E. Mastorakos, and A. P. Dowling, "Experimental and numerical investigation into the propagation of entropy waves," AIAA J. **55**, 446 (2017).
[19] S. Moreau, C. Becerril, and L. Gicquel, "Large-eddy-simulation prediction of indirect combustion noise in the entropy wave generator experiment," Int. J. Spray Combust. Dyn. **10**, 154–168 (2017).
[20] J. Rodrigues, A. Busseti, and S. Hochgreb, "Numerical investigation on the generation, mixing and convection of entropic and compositional waves in a flow duct," J. Sound Vib. **472**, 115155 (2020).
[21] B.-T. Chu and L. S. G. Kovásznay, "Non-linear interactions in a viscous heat-conducting compressible gas," J. Fluid Mech. **3**, 494–514 (1958).
[22] U. Piomelli and J. Liu, "Large-eddy simulation of rotating channel flows using a localised dynamic model," Phys. Fluids **7**, 839–848 (1995).
[23] D. Fredrich, W. P. Jones, and A. J. Marquis, "Thermo-acoustic instabilities in the PRECCINSTA combustor investigated using a compressible LES-*pdf* approach," Flow, Turbul. Combust. **106**, 1399 (2020).
[24] W. P. Jones and V. N. Prasad, "Large eddy simulation of the Sandia flame series (D–F) using the Eulerian stochastic field method," Combust. Flame **157**, 1621–1636 (2010).
[25] Y. Gong, W. P. Jones, and A. J. Marquis, "Study of a premixed turbulent counter-flow flame with a large eddy simulation method," Flow, Turbul. Combust. **106**, 1379 (2021).
[26] D. Noh, E. Karlis, S. Navarro-Martinez, Y. Hardalupas, A. M. K. P. Taylor, D. Fredrich, and W. P. Jones, "Azimuthally-driven subharmonic thermoacoustic

© Author(s) 2021

instabilities in a swirl-stabilised combustor," Proc. Combust. Inst. **37**, 5333–5341 (2019).
[27]D. Fredrich, W. P. Jones, and A. J. Marquis, "The stochastic fields method applied to a partially premixed swirl flame with wall heat transfer," Combust. Flame **205**, 446–456 (2019).
[28]C. S. Yoo, Y. Wang, A. Trouvé, and H. G. Im, "Characteristic boundary conditions for direct simulations of turbulent counterflow flames," Combust. Theory Modell. **9**, 617–646 (2005).
[29]G. Lodato, P. Domingo, and L. Vervisch, "Three-dimensional boundary conditions for direct and large-eddy simulation of compressible viscous flows," J. Comput. Phys. **227**, 5105–5143 (2008).
[30]E. Balaras, C. Benocci, and U. Piomelli, "Two-layer approximate boundary conditions for large-eddy simulations," AIAA J. **34**, 1111–1119 (1996).
[31]A. A. Draad, G. D. C. Kuiken, and F. T. M. Nieuwstadt, "Laminar–turbulent transition in pipe flow for Newtonian and non-Newtonian fluids," J. Fluid Mech. **377**, 267–312 (1998).
[32]E. O. Rolland, F. De Domenico, and S. Hochgreb, "Theory and application of reverberated direct and indirect noise," J. Fluid Mech. **819**, 435–464 (2017).
[33]F. De Domenico, E. O. Rolland, and S. Hochgreb, "A generalised model for acoustic and entropic transfer function of nozzles with losses," J. Sound Vib. **440**, 212–230 (2019).

© Author(s) 2021